Research Square

Preprints are preliminary reports that have not undergone peer review.
They should not be considered conclusive, used to inform clinical practice,
or referenced by the media as validated information.

Nanoplastics reshape local intracellular RNP environments and P-body dynamics

Tatsuhisa Tsuboi

ttsuboi@sz.tsinghua.edu.cn

Tsinghua Shenzhen International Graduate School https://orcid.org/0000-0003-3249-030X

Xiquan Pang

Tsinghua Shenzhen International Graduate School https://orcid.org/0009-0001-3513-3466

Naeem Hussain

Tsinghua Shenzhen International Graduate School

Jiali Ji

Tsinghua Shenzhen International Graduate School

Jiaqi Shen

Tsinghua Shenzhen International Graduate School

Haohang Lin

Tsinghua Shenzhen International Graduate School

Article

Keywords: nanoplastic, P-body, mitochondria, spatial omics, phenotypic profiling

Posted Date: September 11th, 2026

DOI: https://doi.org/10.21203/rs.3.rs-10756134/v1

License: This work is licensed under a Creative Commons Attribution 4.0 International License.
Read Full License

Additional Declarations: There is **NO** Competing Interest.

Abstract

Nanoplastics are biologically active environmental particles, yet how they perturb intracellular organization before overt toxicity remains poorly understood. Here we show that nanoplastic exposure generates spatially restricted RNA–protein states that are largely obscured by whole-cell measurements. Polystyrene and polyethylene terephthalate nanoplastics induced cellular phenotypes distinct from canonical mitochondrial perturbations. Polystyrene-rich cytoplasmic regions were enriched in RNA-binding and P-body-associated proteins, together with transcripts involved in RNA processing and ribonucleoprotein organization, whereas whole-cell transcriptomics predominantly revealed broader stress-response programs. This local molecular reorganization was accompanied by time-dependent remodeling of DDX6-positive P-bodies in intestinal and respiratory epithelial cells. Recurrent motifs within locally enriched transcripts guided the design of RNA oligonucleotides that attenuated nanoplastic-associated P-body remodeling and improved cell viability. These findings identify spatial RNA–protein reorganization as an early feature of the intracellular nanoplastic response and show that locally enriched RNA sequence information can be harnessed to modulate particle-associated cellular dysfunction.

Introduction

Nanoplastics are emerging environmental particles that enter epithelial tissues and elicit diverse cellular responses. Plastic materials can release sub-100 nm particles during routine use[1], and have been detected in human blood, lung tissue, atheromatous plaques, and brain specimens[2–5]. Micro- and nanoplastics have been associated with oxidative stress, inflammatory signaling, mitochondrial dysfunction, altered cell viability, and tissue pathology[6–12]. However, these effects have largely been defined through bulk or late-stage measurements, including transcriptomic responses, reactive oxygen species production, cytokine induction, and cell death. How nanoplastics perturb intracellular organization at earlier stages of cellular exposure remains poorly understood.

Once internalized, nanoparticles encounter a spatially organized cytoplasm containing RNAs, RNA-binding proteins, ribosomes, organelles, and dynamic ribonucleoprotein assemblies. Biomolecular coronas formed by surface-associated macromolecules shape nanoparticle identity and biological activity. For nanoplastics, protein coronas influence cellular recognition and uptake[13], modulate biological effects[14], and correlate with epithelial toxicity[15]. Yet intracellular particle–biomolecule interactions occur within a highly compartmentalized environment in which molecular function depends strongly on spatial context[16,17]. Whether nanoplastic-rich cytoplasmic regions acquire distinct RNA–protein environments, and how such local organization relates to cellular responses, remains unknown.

Ribonucleoprotein (RNP) granules provide a potential interface between local molecular perturbations and cell-wide regulation. RNA localization spatially organizes gene expression in processes ranging from cell polarity and development to synaptic function and organelle-specific protein targeting[18], whereas

membraneless organelles dynamically concentrate RNAs and RNA-binding proteins[19,20]. P-bodies are cytoplasmic RNP assemblies involved in mRNA repression, storage, and turnover, and their formation is sensitive to RNA availability[21]. DDX6 and associated scaffold proteins regulate P-body assembly, composition, and their interactions with other RNA granules[22–24] and P-body-like condensates have also been linked to inflammatory signaling and mammalian mRNA-processing regulation[25]. These properties raise the possibility that intracellular nanoplastics perturb the balance between soluble and assembled RNA–protein states by reshaping local RNP environments.

Here we investigate how nanoplastics reshape local molecular organization within the intracellular environment. Using image-based phenotypic profiling, we show that polystyrene (PS-COOH) and polyethylene terephthalate (PET-COOH) nanoplastics induce cellular states that are distinct from canonical mitochondrial perturbations in intestinal and lung epithelial cells. We then combine whole-cell transcriptomics with fluorescence-guided subcellular proteomics and local RNA profiling to distinguish global stress responses from molecular features associated with nanoplastic-rich cytoplasmic regions. PS-rich regions are enriched in RNA-binding and P-body-associated proteins, together with transcripts involved in RNA processing and RNP organization, revealing a spatially restricted molecular environment that is obscured by whole-cell measurements. Live-cell imaging further shows time-dependent remodeling of DDX6-positive P-bodies, providing a dynamic cellular correlate of this local RNP state. Finally, recurrent motifs within locally enriched transcripts guide the design of RNA oligonucleotides that improve viability and attenuate PS-associated P-body phenotypes. Together, these findings reveal a spatially organized RNP environment associated with intracellular nanoplastics and show that particle-rich intracellular microenvironments can contain functionally informative molecular features.

Results

Image-based phenotypic profiling distinguishes early nanoplastic-associated states from canonical mitochondrial perturbations

Mitochondrial dysfunction is a recurrent feature of nanoplastic exposure. Micro- and nanoplastics have been associated with oxidative stress, inflammatory signaling, mitochondrial dysfunction, and loss of cellular homeostasis [6,8–10]. However, mitochondria integrate bioenergetic, metabolic, calcium, and stress-signaling inputs and therefore represent a common convergence point for diverse cellular insults [26]. Consistent with this, live-cell analysis of intestinal organoids has shown that nanoplastic internalization can occur without reproducible changes in mitochondrial polarization, mitochondrial mobility, or cellular ATP [27]. Thus, although mitochondrial dysfunction may emerge during sustained nanoplastic exposure, whether it represents an early and primary cellular response remains unclear.

To capture early phenotypic changes that might not be apparent from static morphology alone, we combined z-stack imaging of cellular and mitochondrial features with time-resolved measurements of

mitochondrial motion (Fig. 1a). Cells were exposed to PS-COOH or PET-COOH at 125 μg/ml, a concentration that did not measurably reduce cell viability under our experimental conditions, allowing us to examine cellular responses before overt loss of fitness. We compared these nanoplastic treatments with gold nanoparticle controls and 25 reference perturbagens spanning inhibitors of mitochondrial fission and fusion, organelle uncouplers, mitochondrial DNA stress inducers, membrane-potential disrupters, electron-transport-chain inhibitors, and reactive oxygen species regulators (Fig. 1b). Three-channel z-stack images reporting mitochondrial morphology, membrane-potential-associated fluorescence, and nuclear morphology were integrated with time-resolved mitochondrial motion to generate single-cell phenotype representations (Fig. 1a, b and Supplementary Fig. 1). To complement the analysis of these high-dimensional images, we performed classification-based feature analysis. In A549 cells, incorporating mitochondrial motion improved phenotype classification compared with using z-stack appearance features alone, increasing top-1 accuracy from 51.32% to 57.57% and macro-F1 from 51.27% to 55.99% (Supplementary Fig. 2).

Feature-space visualization demonstrated that PS-COOH- and PET-COOH-treated cells populated regions distinct from the primary distribution generated by standard mitochondrial perturbagens and nanoparticle controls (Fig. 1c). Representative endpoint images showed corresponding differences in cellular and mitochondrial morphology relative to the reference conditions (Fig. 1d). Similar pattern of organization was observed in both the NCM460 and A549 models, demonstrating that nanoplastic exposure resulted in a reproducible early multidimensional phenotype. (Supplementary Fig. 3). Together, these results show that the early cellular states induced by PS-COOH and PET-COOH are not readily classified as canonical mitochondrial perturbations represented in our reference panel. Thus, during the first 6 h of exposure, nanoplastics generate a distinct multiparametric phenotype rather than a response dominated by established forms of mitochondrial dysfunction.

Subcellular proteomics reveals local enrichment of P-body-associated proteins not captured by bulk transcriptomics

The early nanoplastic-associated phenotypes identified by image-based profiling differed from those induced by the reference mitochondrial perturbations examined above, suggesting distinct intracellular processes contribute to the initial cellular response. We therefore asked whether nanoplastic exposure is associated with spatially restricted molecular changes that would be obscured by whole-cell measurements. Since subcellular localization can reveal changes in molecular organization without corresponding changes in total cellular abundance, we used the Yokogawa Single Cellome SS2000 platform, which enables microscope-guided subcellular capillary sampling of defined regions within live cells [28], to compare the molecular composition of fluorescence-defined PS-rich and PS-poor cytoplasmic regions in NCM460 cells (Fig. 2a). Spatial profiling was limited to PS-COOH in NCM460 cells because the available PET-COOH particles contained a polystyrene component introduced during their template-based synthesis, precluding unambiguous identification of PET-specific particle-rich regions.

Across 863 detected proteins, comparison of PS-rich and PS-poor regions revealed enrichment of multiple RNA-binding and RNA-granule-associated proteins (Fig. 2b). DDX6 was consistently enriched in PS-rich regions across two biological replicates, together with additional proteins associated with cytoplasmic ribonucleoprotein granules. DDX6 is a core P-body-associated DEAD-box RNA helicase that regulates P-body assembly, composition, and interactions with other cytoplasmic RNA granules [22,23]. P-body assembly is also sensitive to RNA availability [21]. Together, these findings identified the local enrichment of P-body-associated proteins as a prominent molecular feature of PS-rich cytoplasmic regions.

We next asked whether this local RNP-associated signature was reflected in the whole-cell transcriptional response to nanoplastic exposure. Bulk RNA sequencing of NCM460 cells after 24 h exposure to PS-COOH or PET-COOH revealed broad stress-response programmes (Fig. 2c). Gene Ontology analysis showed enrichment of antiviral and innate-immune responses, RIG-I-like receptor signalling, responses to chemical and oxidative stress, and endoplasmic-reticulum stress pathways relative to control cells (Fig. 2d). Representative responsive transcripts included *IFIT2*, *IFIT3*, *OAS2*, and *IFIH1* (Fig. 2f). The oxidative- and endoplasmic-reticulum-stress signatures were consistent with previously reported nanoplastic responses [6,9], while RNA-regulatory changes, including altered intestinal miRNA profiles, have also been reported following PS nanoplastic exposure [11]. PET-COOH elicited a partially overlapping transcriptional response, including antiviral and xenobiotic-response categories (Fig. 2e,f).

Despite these broad stress-associated transcriptional changes, canonical P-body components were not coordinately upregulated at the whole-cell RNA level. *DDX6*, *EDC4*, *LSM14A*, *LSM14B* and *NBDY* showed no concerted increase following either PS-COOH or PET-COOH exposure (Fig. 2g–i). Thus, the local enrichment of *DDX6* and other RNA-granule-associated proteins in PS-rich cytoplasmic regions occurred without a corresponding transcriptional increase in major P-body components. Together, these data distinguish two levels of the nanoplastic response: a broad stress program detectable by whole-cell transcriptomics and a spatially restricted enrichment of P-body-associated proteins in PS-rich cytoplasmic regions. The dissociation between localized protein enrichment and whole-cell transcript abundance is consistent with the spatial reorganization of RNA–protein assemblies rather than transcriptional upregulation of P-body components.

Polystyrene exposure remodels DDX6-positive P-bodies

Nanoneedle sampling identified a spatially restricted P-body-associated protein signature in PS-rich regions that was not evident from whole-cell transcriptomic profiling. We therefore asked whether this local molecular feature was accompanied by measurable changes in P-body dynamics during PS exposure. DDX6-positive P-bodies are dynamic RNA–protein assemblies whose abundance and size are sensitive to the pool of non-translating cytoplasmic RNA [21,23]. We tracked DDX6-EGFP-positive P-bodies

in living NCM460 cells after PS addition and quantified the puncta numbers, mean punctum area, and cell-area-normalized punctum density over 360 min (Fig. 3 and Supplementary Fig. 4).

PS exposure progressively altered the DDX6-positive P-body phenotype. At 360 min, PS-treated NCM460 cells contained 12.94 ± 0.50 puncta per cell compared with 7.64 ± 0.36 in the control, corresponding to an increase of approximately 5.31 puncta per cell (Fig. 3c). Mean punctum area decreased from 1.312 ± 0.037 μm² in control cells to 0.835 ± 0.026 μm² after PS exposure (Δ ≈ −0.48 μm²; Fig. 3d), while punctum density increased from 0.02363 ± 0.00120 to 0.03897 ± 0.00132 μm^{-2} (Δ ≈ +0.02 μm^{-2}; Fig. 3e). Together, these changes shifted the population towards more numerous and denser DDX6-positive puncta with a smaller mean area. The same directional pattern was observed in independently analyzed A549 cells, in which PS exposure increased DDX6-positive puncta number and density while reducing mean punctum area (Supplementary Fig. 5). Together, the spatial-omics (Fig. 2b) and live-cell imaging results (Fig. 3a) showed that DDX6-positive P-bodies undergo remodeling upon PS exposure, with increasing puncta number and density and decreasing mean punctum area. Coupled with the local enrichment of P-body-associated proteins in PS-rich cytoplasmic regions, these findings position DDX6-positive P-body remodeling as an early membraneless-compartment response to nanoplastic exposure.

Local RNA profiling of PS-rich cytoplasmic regions identifies recurrent sequence motifs for MRO design

Given the local enrichment of P-body-associated proteins and the remodeling of DDX6-positive P-bodies following PS exposure, we asked whether PS-rich cytoplasmic regions also contained a distinct RNA population. We therefore applied the same fluorescence-guided subcellular sampling strategy used for local proteomics to isolate RNA from fluorescence-defined PS-rich and PS-poor cytoplasmic regions of NCM460 cells for RNA sequencing (Fig. 4a, Supplementary Fig. 6). Among 3,890 detected mRNAs, 207 were enriched in PS-rich regions and 11 in PS-poor regions at the thresholds used for analysis (Fig. 4b,c). Gene Ontology analysis of the PS-rich transcript set showed enrichment of pathways related to translation initiation, RNA processing, ribonucleoprotein-complex biogenesis, protein–RNA complex assembly, and ribosome-associated functions (Fig. 4d). These functional categories paralleled the RNP-associated protein signature identified by local proteomics. Thus, PS-rich cytoplasmic regions contained a distinct transcript population enriched for RNA-processing and ribonucleoprotein-associated functions.

We next asked whether recurrent sequence features within the locally enriched transcript population could be used to generate defined RNA oligonucleotide candidates. Because RNA sequence and structural features can influence interactions with RNA-binding proteins and the organization of ribonucleoprotein assemblies [29,30], we performed motif analysis on a broader transcript-level set of 459 sequences enriched in PS-rich regions, as defined by the criteria described in the Methods (Fig. 4e and Supplementary Fig. 7). MEME/FIMO (Multiple EM for Motif Elicitation/Find Individual Motif Occurrences) analysis identified five recurrent motifs. Three were selected for functional testing on the basis of motif length, recurrence, and sequence complexity. A 21-nt motif was excluded because of its shorter length,

whereas a 28-nt poly(A)-rich motif was excluded because of its low sequence complexity. The remaining three motifs, each 29–30 nt in length, were designated MRO-1, MRO-2, and MRO-3 (Fig. 4e,f). For cellular testing, the corresponding motif-derived RNA oligonucleotides were chemically stabilized using terminal phosphorothioate linkages and 2'-fluoro substitutions; their sequences and chemical modifications are provided in Supplementary Table 2. Together, fluorescence-guided local RNA profiling identified a transcript population enriched in RNA-processing and ribonucleoprotein-associated functions within PS-rich cytoplasmic regions. Recurrent sequence motifs within this population were used to generate three defined motif-derived RNA oligonucleotides for subsequent functional testing.

Motif-derived RNA oligonucleotides attenuate PS-associated P-body phenotypes and improve cell viability

Having identified recurrent RNA sequence motifs within PS-rich cytoplasmic regions, we asked whether the corresponding motif-derived RNA oligonucleotides (MROs) could attenuate the PS-associated cellular phenotypes described above. NCM460-DDX6-EGFP cells were analyzed under four matched conditions for each RNA: mock control, MRO or tRNA alone, PS alone, and PS plus the corresponding RNA. Responses were assessed by cell viability at 24 h and by time-resolved imaging of DDX6-positive P-bodies over 410 min (Fig. 5a,b,d–g). All three MROs increased cell viability relative to PS alone, whereas tRNA did not produce a significant effect (MRO-1, $q = 0.0040$; MRO-2, $q = 0.0323$; MRO-3, $q = 0.0040$; tRNA, $q = 0.2163$; Fig. 5c). None of the MROs measurably reduced baseline viability when administered alone relative to the mock control (MRO-1, $q = 0.3950$; MRO-2, $q = 0.6231$; MRO-3, $q = 0.3606$), and tRNA alone was likewise unchanged ($q = 0.5603$). Thus, the three independently selected MROs improved viability under PS exposure without an evident effect on baseline viability.

Time-resolved P-body imaging revealed a complementary response (Fig. 5d–g). Following the initial transition from a common starting state, mock-control and MRO-only cells remained within a lower DDX6-positive puncta-count range, whereas PS exposure produced a substantial increase. Co-treatment with MRO-1, MRO-2, or MRO-3 shifted the PS-associated trajectories towards the control range. At 410 min, all three MROs reduced DDX6-positive puncta number relative to PS alone ($q = 0.0006$, 0.00454 and 0.0258 for MRO-1, MRO-2, and MRO-3, respectively), corresponding to a decreases of 5.0, 3.9 and 3.2 puncta per cell. MRO-1 produced the largest effect, whereas MRO-2 and MRO-3 produced intermediate attenuation. By contrast, tRNA produced a modest reduction of 2.2 puncta per cell that did not reach significance ($q = 0.071$). These results indicate that the MROs preferentially attenuated the PS-associated increase in P-body number rather than producing a general effect on baseline P-body abundance.

The effects were not uniform across all P-body parameters. In NCM460 cells, mean punctum area showed little change following MRO co-treatment (Supplementary Fig. 8a–d), whereas MRO-1 and MRO-2 reduced PS-associated punctum density towards the control range (Supplementary Fig. 8e–h). We next tested whether MROs designed from NCM460 local RNA profiles retained activity in A549 cells. In

this independent epithelial model, MRO-2 and MRO-3 produced significant attenuation of the PS-associated puncta count, whereas effects on mean punctum area were modest (Supplementary Figs. 9). Across both cell models, puncta number was therefore the most consistently MRO-responsive P-body readout. Together, these results show that motif-derived RNA oligonucleotides designed from recurrent sequences enriched in PS-rich cytoplasmic regions can improve viability and attenuate selected PS-associated P-body phenotypes. The concordance between the local RNA-derived sequence information and the live-cell phenotypic response provides functional evidence that sequence features within the PS-associated RNA signature can be used to modulate nanoplastic-associated cellular states.

Discussion

Our study reveals a spatially organized RNA–protein response associated with the intracellular environment of nanoplastics. Biological effects of micro- and nanoplastics have largely been characterized through downstream outcomes such as oxidative stress, mitochondrial dysfunction, inflammatory signaling, and loss of cellular fitness [6,8–10]. These responses are important indicators of toxicity, but they provide limited information about how nanoscale plastic particles initially perturb the molecular organization of the cell. By positioning PS-COOH and PET-COOH against a defined panel of mitochondrial perturbations, our image-based analysis showed that the early nanoplastic-associated phenotype was distinct from the canonical mitochondrial states represented in this reference space. This does not exclude mitochondrial involvement; rather, because mitochondria integrate metabolic, bioenergetic, calcium, and stress signals, mitochondrial abnormalities may emerge as part of a broader response rather than uniquely defining the initial interaction [26]. This interpretation is consistent with reports that nanoplastic internalization can occur without reproducible changes in mitochondrial polarization, movement, or cellular ATP under specific conditions [27], and that anionic PS nanoplastics can rapidly induce non-mitochondrial responses such as VE-cadherin and actin remodeling [31]. Together, these observations motivate a view of intracellular nanoplastic exposure in which localized molecular reorganization accompanies, and may precede, conventional organelle- and stress-associated phenotypes.

Our spatial molecular analyses point to RNA–protein organization as one such process. Nanoparticle surfaces are known to acquire biological identity through associated macromolecules [13–15], while RNAs and proteins continuously redistribute among organelles, soluble complexes and cytoplasmic granules during cellular stress [32]. In our study, fluorescence-defined PS-rich cytoplasmic regions were enriched in RNA-binding and RNA-granule-associated proteins, including DDX6. By contrast, whole-cell transcriptomics predominantly captured broader antiviral, innate-immune, oxidative and endoplasmic-reticulum stress programs. Canonical P-body transcripts were not coordinately induced at the whole-cell level, suggesting that the P-body-associated signature arose through local molecular enrichment rather than transcriptional activation of a P-body gene program. Thus, image-guided nanoneedle sampling revealed a local–bulk divergence that would be difficult to detect by whole-cell averaging. Consistent with the idea that intracellular nanoplastic interfaces can organize spatially restricted molecular

environments, proximity-labeling studies using a different PS nanoparticle system have identified distinct protein populations near internalized particles[33]. Our findings extend this concept to RNA biology by showing that PS-rich intracellular regions are enriched in RNA-binding and RNA-granule-associated factors, identifying RNA-handling machinery as a prominent feature of the local molecular response.

DDX6-positive P-bodies provided a dynamic cellular correlate of this spatial RNP signature. DDX6 is a central regulator of P-body assembly and composition [22,23], and P-body organization is sensitive to cytoplasmic RNA abundance and translational state [21]. PS exposure increased the number and density of DDX6-positive puncta while reducing their mean size, with the same directional response in two epithelial cell models. These imaging data connect the spatial molecular signature to a directly observed, time-resolved change in cytoplasmic organization. P-bodies are dynamic post-transcriptional compartments whose RNA content and physical state can change rapidly in response to cellular conditions [34–36]. The shift towards more numerous, smaller DDX6-positive assemblies is therefore consistent with altered partitioning among P-body states rather than simple accumulation of granule material. A recent study using a distinct synthetic nanoparticle system similarly observed contacts between intracellular nanoparticles and P-bodies or stress granules and, in rare cases, the formation of RNA- and protein-containing condensate coronas[37]. Together, these observations support the idea that intracellular particles can influence the organization of dynamic RNP compartments. Our findings establish an in situ association between PS-rich intracellular microenvironments and remodeling of DDX6-positive P-bodies.

The local RNA data further connect this P-body phenotype to sequence-level information. Transcripts enriched in PS-rich regions were associated with RNA processing, translation and RNP-complex functions, extending the spatial proteomic signature to the RNA layer. Because RNA sequence and structure can influence RNA–protein interactions and partitioning into RNP assemblies[29], we used recurrent motifs within these transcripts to design three chemically stabilized motif-derived RNA oligonucleotides (MROs). All three MROs improved viability in PS-exposed NCM460 cells and attenuated the PS-associated increase in DDX6-positive punctum number, whereas tRNA did not reproduce these significant effects. MRO-only conditions remained close to untreated or mock controls for the principal viability and P-body-count measurements, indicating that the oligonucleotides preferentially affected the PS-associated state rather than broadly perturbing cells on their own. The effects were also selective across P-body measurements: punctum number was consistently responsive, whereas mean punctum area changed less strongly. These findings suggest that sequence information contained in locally enriched RNAs can selectively modulate the PS-associated cellular state.

Sequence-defined oligonucleotides can act as molecular competitors in biological and therapeutic contexts [30], suggesting that the MROs may modulate interactions with RNA-binding proteins or alter local RNA–protein stoichiometry. Previous studies have also shown that extracellular protein coronas can modify specific PS-associated cellular effects [14,38]. Our approach extends this concept to the intracellular RNA environment by deriving sequence-defined oligonucleotides from RNAs enriched within

PS-rich cytoplasmic regions and testing their ability to modulate PS-associated viability and P-body phenotypes. The ability of these MROs to improve cellular fitness and attenuate selected P-body changes indicates that spatially enriched RNA sequences contain functional information that can influence the cellular response to nanoplastic exposure. More broadly, these findings suggest that sequence-defined RNAs can be used to probe and modulate nanoplastic-responsive RNP states, providing a route from spatial molecular profiling to functional modulation of intracellular RNP organization.

An important limitation of our spatial approach is the very small amount of biological material obtained from subcellular regions, representing only a fraction of a single cell. Although this enables high spatial specificity, it limits molecular coverage and can increase sensitivity to sampling variability, particularly for low-abundance RNAs and proteins. The regional datasets therefore capture major features of local molecular organization rather than its full composition. Higher-throughput and more sensitive spatial profiling should enable deeper characterization of these particle-associated microenvironments.

More broadly, our results suggest that the biological consequences of intracellular nanoscale particles depend not only on changes in whole-cell pathway activity, but also on the molecular environments associated with particle-rich regions. Fluorescence-guided regional sampling revealed an RNP-associated state that was largely obscured by whole-cell measurements, while live-cell imaging connected this spatial signature to remodeling of a dynamic RNA–protein compartment. Motif-derived RNA oligonucleotides further showed that sequence information recovered from the locally enriched RNA population can be used to modify selected particle-associated cellular phenotypes. By integrating particle-guided subcellular sampling, spatial molecular profiling, live-cell imaging, and sequence-informed functional testing, our study provides a framework for resolving how persistent nanoscale objects reshape intracellular molecular organization. These findings extend the biological characterization of nanoplastics beyond bulk toxicity and organelle dysfunction by identifying spatially organized RNA–protein environments as a previously underappreciated dimension of the intracellular nano–biointerface.

Methods

Cell culture

NCM460 cells (Cellosaurus, CVCL_0460) and A549 cells (ATCC, CCL-185) were maintained in RPMI 1640 medium (CellorLab, CB004) supplemented with 10% fetal bovine serum (VisionEstern, catalog no. VE10088802) and 1% penicillin–streptomycin at 37°C with 5% CO_2. Cells were passaged using 0.25% trypsin–EDTA (CellorLab, CB011). Cultures were routinely monitored for mycoplasma contamination using a one-step rapid mycoplasma detection kit (Biosharp, BL1471A).

Lentivirus production and transduction

Lentivirus was produced in HEK293T cells (ATCC, CRL-3216) by co-transfection with the pHAGE-hDDX6-eGFP-FLAG, encoding human DDX6 fused at its C-terminus to EGFP–FLAG through a 4GS linker under the EF-1α promoter, psPAX2 (Addgene, 12260) and pMD2.G (Addgene, 12259) using Lipo8000 transfection reagent (Beyotime, C0533). Virus-containing medium was collected after 72 h and passed through a 0.45-μm filter. NCM460 and A549 cells were transduced for 48 h with 10 μg/ml polybrene (Beyotime, C0531); EGFP-positive cells were isolated by fluorescence-activated cell sorter and maintained as polyclonal populations. DDX6–EGFP expression was verified by fluorescence microscopy and flow cytometry.

Nanoplastic, nanoparticle and drug preparation and treatment

Fluorescent 50-nm carboxylated polystyrene (PS-COOH; Bioty Science, ABTR-0005-COOH) and polyethylene terephthalate (PET-COOH; Bioty Science, BPET-0005-COOH) nanoplastics, containing fluorophores embedded within the particles, were supplied as 10mg/ml aqueous suspensions and diluted to 125 μg/ml in complete culture medium before use. This concentration did not cause detectable loss of viability during the early imaging window, although reduced viability was evident after 24 h. Citrate-reduced 50-nm gold (Au) nanoparticles were used at the same concentration as a nanoparticle comparator. The 25 mitochondrial perturbagens, together with their sources, identifiers and working concentrations, are listed in Supplementary Table 1.

Image acquisition

Cells were seeded at 13,000 cells per well in poly-L-lysine-coated 96-well glass-bottom plates (Cellvis, P96-1.5H-N) and cultured for 24 h. Plates were coated with 0.1 mg/ml poly-L-lysine (Beyotime, ST509). Before imaging, cells were incubated for 30 min with Hoechst 33342 (Beyotime, C1022; 2.5 μg/ml), MitoTracker Deep Green FM (Yeasen, 40742ES50; 25 nM) and tetramethylrhodamine ethyl ester (TMRE; Aladdin, T131055; 25 nM), washed once with DPBS (Bioshrap, BL310A) and exposed to the indicated treatment listed in Supplementary Table 1 at the start of acquisition.

Images were acquired on a Nikon Eclipse Ti2-E microscope with a Yokogawa CSU-X1 spinning-disk confocal unit and a Plan Apo 40×/0.95 air objective. Each 940 × 680-pixel field was collected at 0.275 μm per pixel as 27 z-sections at 0.4-μm intervals. Nine time points were acquired at 45-min intervals from 0 to 360 min using constant settings within each experiment. The far-red particle channel acquired for PS-COOH and PET-COOH samples was excluded from phenotype classification.

Image-based phenotype classification and feature-space analysis

To quantitatively characterize treatment-induced cellular phenotypes, single cells were segmented using Cellpose v.4.0[39] and tracked across the time series by trackastra[40]; NCM460 and A549 datasets were processed independently. Phenotype-stratified training, validation, and test sets were assigned at a 70:10:20 ratio. A deep learning-based phenotype classification framework was used to examine

multichannel z-stack images that described mitochondrial morphology, mitochondrial membrane potential-associated fluorescence, and nuclear morphology. The model acquired volumetric appearance features from three-channel z-stack images before incorporating mitochondrial motion information obtained from the mitochondrial channel via dense optical flow. The appearance and motion data were then combined to generate a single-cell phenotypic representation to facilitate classification.

The appearance model was trained before optimizing the motion incorporation component with the Adam optimizer and cosine learning-rate annealing. Using independent validation and test datasets, classification performance was measured using top-1 accuracy, top-5 accuracy, macro-precision, macro-recall, and macro-F1 scores. The learned feature representations were simulated into a two-dimensional space using Uniform Manifold Approximation and Projection (UMAP) [41], enabling the visualization of phenotypic correlations between nanoplastic-treated cells and standard perturbations. Hyperparameters and other detailed technical information are summarized in the supplementary methods.

Bulk RNA sequencing

Cells were treated with PS-COOH, PET-COOH, or Au nanoparticles at 125 μg /ml for 24 h. Three independent biological replicates were prepared for each condition. Total RNA was extracted from independently cultured samples and submitted to BGI Genomics (Shenzhen, China) for library preparation and sequencing. Poly(A)-enriched RNA libraries were sequenced on a DNBSEQ platform using 150-bp paired-end reads. Raw reads were filtered for adaptor contamination, low quality, ambiguous bases, poly (X) tracts, and read length using SOAPnuke.

Fluorescence-guided subcellular sampling

NCM460 cells were cultured in glass-bottom confocal dishes (NEST, catalog no. 801001) coated with 0.1 mg/ml poly-L-lysine (Beyotime, ST509) and exposed to 125 μg/ml PS-COOH for 24 h. Nile blue encapsulated within the PS-COOH is introduced through the manufacturing process and excited using a 640 laser. NCM460 cells were selected for subcellular sampling because their relatively large size and firm adherence allowed fluorescence-defined particle-rich and particle-poor cytoplasmic regions to be spatially resolved under a 40× objective and reproducibly sampled by pressure-controlled capillary aspiration. PS-rich and PS-poor cytoplasmic regions were defined according to particle-associated fluorescence and sampled from individual cells using the Single Cellome SS2000 system (Yokogawa) for downstream proteomics or transcriptomics analysis.

Nanoneedle-based subcellular proteomics

Two pooled samples were collected per regional group, each comprising six regions from six different cells. Samples were lysed in 1% sodium deoxycholate in 100 mM Tris–HCl (pH 8.5), reduced with tris(2-carboxyethyl)phosphine, alkylated with chloroacetamide, and digested overnight at 37°C with trypsin at a 1:50 enzyme-to-protein ratio. Peptides were acidified and desalted using SDB-RPS material.

Peptides were separated on a Vanquish Neo UHPLC system using a μPAC Nseo High Throughput column with a 13.5-min gradient and analyzed by data-independent acquisition on an Orbitrap Astral

mass spectrometer. DIA data were acquired over 380–980 m/z using 2-Th isolation windows and a 0.6-s cycle time.

Raw data were processed with DIA-NN v.1.9.2 in library-free mode against the human UniProt reference proteome (13 January 2025). Searches used Trypsin/P specificity with up to two missed cleavages, fixed cysteine carbamidomethylation, variable methionine oxidation and protein N-terminal acetylation, and 15-p.p.m. mass accuracy. Match-between-runs was enabled, precursor false discovery rate was controlled at 1%, and protein abundances were quantified using MaxLFQ. Missing values were imputed near the measured detection limit, and proteins with at least 50% valid measurements in either group were retained. Pairwise PS-rich/PS-poor log2 abundance ratios were calculated separately for the two sample pairs. RNA-granule, RNA-binding and P-body-associated proteins were annotated using RNAgranuleDB.

Nanoneedle-based subcellular transcriptomics

Three pooled samples were collected per regional group, each containing three regions from three different cells. First-strand cDNA synthesis and whole-transcriptome amplification were performed using the Discover-sc WTA Kit V2 (Vazyme, N711), and approximately 1ng of amplified cDNA was used for library preparation with the TruePrep DNA Library Prep Kit V2 for Illumina (Vazyme, TD503). Libraries were sequenced by Novogene (Beijing, China) on an Illumina platform. Raw reads were filtered using fastp v.0.23.1 before downstream analysis.

RNA sequencing and data analysis

Sequence processing used the nf-core/rnaseq[42,43] workflow listed in Supplementary Table 3. RSEM transcript-level abundance estimates were imported into R with tximport using lengthScaledTPM and analyzed with DESeq2[44]. Genes with at least 10 counts in at least two samples were retained, and Benjamini–Hochberg correction was applied.

For bulk RNA sequencing, log2 fold changes were shrunk with apeglm. Transcripts with average expression > 10, absolute log2 fold change > 0.3 and adjusted $P < 0.01$ were retained for downstream analysis, and Gene Ontology enrichment was performed with clusterProfiler[45] and org.Hs.eg.db. For nanoneedle RNA sequencing, upregulated transcripts meeting average expression > 10, log2 fold change > 0.3, and adjusted $P < 0.01$ were used for motif analysis.

Motif discovery and RNA oligonucleotide design

Motifs were discovered in the threshold-filtered nanoneedle RNA-seq transcript set using MEME[46] and assessed with Find Individual Motif Occurrences[47] (FIMO). Three motif-derived RNA oligonucleotides (MRO-1, MRO-2, and MRO-3) were designed from recurrent motif-containing regions and evaluated with RNAfold[48] for predicted secondary structure and minimum free energy. Their exact 5'–3' sequences, lengths and chemical modifications are provided in Supplementary Table 2. Yeast tRNA (Invitrogen,

15401011) served as the control RNA oligonucleotide; MROs and control RNA oligonucleotide were used at 500nM.

Live-cell imaging of P-body

NCM460 and A549 cells stably expressing DDX6–EGFP were seeded at approximately 3 × 10^5 cells per glass-bottom confocal dish (NEST, 801001) coated with 0.1 mg/ml poly-L-lysine (Beyotime, ST509). Cells were imaged at approximately 90% confluence using the imaging module of the Single Cellome SS2000 equipped with a 40×/0.95 air objective.

For direct analysis of the nanoplastic response, cells were exposed to PS-COOH at 125 μg/ml immediately before imaging. Where indicated, 50-nm Au nanoparticles were used at 125 μg/ml as a nanoparticle control. Images were acquired every 10 min for 410 min. Each time point comprised 40 z-sections acquired at 0.5-μm intervals, with a pixel size of 0.1625 μm and an image size of 2,000 × 2,000 pixels. The NCM460 and A549 datasets comprised five and four independent experiments, respectively.

For motif-derived RNA oligonucleotide experiments, cells were analyzed under four matched conditions for each RNA oligonucleotide: untreated control, PS-COOH alone, RNA oligonucleotide alone, and PS-COOH plus RNA oligonucleotide. PS-COOH and RNA oligonucleotide were used at final concentrations of 125 μg/ml and 500 nM, respectively. Images were acquired every 10 min for 410 min, with 15 z-sections collected at each time point over an approximately 7.5-μm z-range. Four fields were acquired per condition in each of 3–5 independent experiments. Acquisition settings were kept constant across conditions within each experiment.

Image-based P-body quantification

We built on and optimized a previously established image analysis pipeline[49]. Cells were segmented and tracked with Cellpose[39]; DDX6–EGFP-positive puncta were detected with Spotiflow[50]. Punctum count, mean punctum area, and punctum density (count divided by segmented cell area) were quantified for each tracked cell at each time point. Local PS enrichment was calculated as mean PS fluorescence around detected puncta divided by mean PS fluorescence within the cell mask.

Fields with acquisition failure, severe drift or poor focus, and cells intersecting image boundaries, absent at time zero, failing segmentation, or failing tracking were excluded. For the MRO endpoint cohort, treatment-blind morphology and quality filters were applied to the first three frames: time-zero cell area between the 5th and 99.5th percentiles, time-zero circularity at or above the 78th percentile, minimum early area ratio ≥ 0.45, and early circularity change and centroid displacement at or below the 99th and 98th percentiles, respectively.

Cell viability assay

Cells were seeded at 5,000 cells per well in 96-well glass-bottom plates (Cellvis, P96-1.5H-N), cultured for 24 h and then exposed for 24 h to 125 μg/ml PS-COOH and 500 nM RNA oligonucleotides, both or

neither. Viability was measured with the CellTiter-Lumi Steady Luminescent Cell Viability Assay Kit (Beyotime, C0069M) according to the manufacturer's instructions using a Tecan Spark plate reader. Values were normalized within each independent experiment to the untreated control. Four independent experiments were performed with one well per condition in each experiment. Wells with luminescence approximately two orders of magnitude below the remaining measurements were excluded according to the assay-quality rule.

Statistical analysis and reproducibility

Sample size was not predetermined statistically, and unless stated otherwise, n denotes an independent culture or plating experiment rather than an individual cell. Treatment well positions were fixed, fields with adequate cell density were selected manually, and operators were aware of treatment identity during acquisition. Image segmentation, tracking, and punctum detection were automated and subject to the quality-control procedures described above.

Unless stated otherwise, data are presented as mean ± s.e.m. and tests were two-sided. RNA-seq differential expression was analyzed with DESeq2[44]. Proteomic PS-rich/PS-poor comparisons were descriptive because two independent pooled samples were available per regional group. Viability comparisons used paired t-tests with the independent plating experiment as the paired unit; pooled cell-level P-body endpoint distributions were compared by Mann–Whitney U tests. P values were adjusted within each comparison family using the Benjamini–Hochberg procedure, with $q < 0.05$ considered significant. Time-resolved pooled-cell trajectories were summarized descriptively. Exact sample sizes and panel-specific tests are reported in the figure legends and source data.

AI-assisted language editing

ChatGPT (OpenAI) was used solely for language editing and proofreading of the manuscript. All scientific content was reviewed and approved by the authors.

Resource availability:

Lead contact

Further information and requests for raw data and reagents should be directed to and will be fulfilled by the lead contact, Tatsuhisa Tsuboi (ttsuboi@sz.tsinghua.edu.cn).

Data and Code Availability

- The single-cell dataset utilized for training the model that distinguishes nanoplastic-induced phenotypic changes from canonical mitochondrial perturbations in A549 and NCM460 cells exposed to canonical mitochondrial perturbations, along with all model weights, is publicly accessible via Zenodo at https://zenodo.org/records/21818886.

- The single-cell dataset utilized for evaluating the effects of motif-derived RNA oligonucleotides on P-bodies in A549 and NCM460 cells exposed to polystyrene, along with the spotiflow model weights, is publicly accessible via Zenodo at https://zenodo.org/records/21817136.
- The code used for image-based phenotype classification and feature-space analysis can be found at https://github.com/naeem5/phenotype-classification.
- The analysis pipeline code related to the analysis of motif-derived RNA oligonucleotides on P-bodies in cells exposed to nanoplastics, including P-body detection and quantification, is available at https://github.com/ggab4364/PBspot_assay.
- Any additional information required to reanalyze the data reported in this paper is available from the lead contact upon request.

Declarations

Acknowledgments:
We thank members of the Tsuboi laboratory for helpful discussions on the paper. Receipt of the pHAGE-hDDX6-eGFP-FLAG plasmid from Dr. W Chen and gold nanoparticles from Dr. C Tan are gratefully acknowledged. We thank the Biopharmaceutical and Health Engineering Research Core Facility, Tsinghua Shenzhen International Graduate School for technical support. We thank A Khan and C Mao for critically reading the manuscript. This work was supported in part by the Key Research and Development Program of the Ministry of Science and Technology 2024YFE0102700, 2023YFA0914303, startup fund OD2021031C, Interdisciplinary Research and Innovation Fund JC2022008, and Overseas Research Cooperation Fund HW2024009 from Tsinghua SIGS (to T.T.).

Author contributions:

X.P. and T.T. conceived and designed the project. X.P., and J.J. performed wet experiments and analyzed image data. X.P., N.H., J.S., and T.T. performed image quantification and computational analysis. X.P. N.H., and T.T. wrote the manuscript.

Declaration of interests:

The authors declare no competing interests.

References

1. Zangmeister CD, Radney JG, Benkstein KD, Kalanyan B (2022) Common single-use consumer plastic products release trillions of sub-100 nm nanoparticles per liter into water during normal use. Environ Sci Technol 56:5448–5455
2. Leslie HA et al (2022) Discovery and quantification of plastic particle pollution in human blood. Environ Int 163:107199

3. Jenner LC et al (2022) Detection of microplastics in human lung tissue using micro-FTIR spectroscopy. Sci Total Environ 831:154907
4. Marfella R et al (2024) Microplastics and nanoplastics in atheromas and cardiovascular events. N Engl J Med 390:900–910
5. Nihart AJ et al (2025) Bioaccumulation of microplastics in decedent human brains. Nat Med 31:1114–1119
6. Lamoree MH et al (2025) Health impacts of microplastic and nanoplastic exposure. Nat Med 31:2873–2887
7. Hu M, Palić D (2020) Micro- and nano-plastics activation of oxidative and inflammatory adverse outcome pathways. Redox Biol 37:101620
8. Lin S et al (2022) Metabolomics reveal nanoplastic-induced mitochondrial damage in human liver and lung cells. Environ Sci Technol 56:12483–12493
9. Wu Q et al (2024) Polystyrene nanoplastics-induced lung apoptosis and ferroptosis via ROS-dependent endoplasmic reticulum stress. Sci Total Environ 912:169260
10. Huang Y et al (2023) Polystyrene nanoplastic exposure induces excessive mitophagy by activating the AMPK/ULK1 pathway in differentiated SH-SY5Y cells and dopaminergic neurons in vivo. Part Fibre Toxicol 20:44
11. Hsu W-H et al (2025) Polystyrene nanoplastics disrupt the intestinal microenvironment by altering bacteria-host interactions through extracellular vesicle-delivered microRNAs. Nat Commun 16:5026
12. Liu Z et al (2023) Anionic nanoplastic contaminants promote Parkinson's disease-associated α-synuclein aggregation. Sci Adv 9:eadi8716
13. Cai R et al (2024) Protein corona-directed cellular recognition and uptake of polyethylene nanoplastics by macrophages. Environ Sci Technol 58:14158–14168
14. Xiao S et al (2024) Protein corona alleviates adverse biological effects of nanoplastics in breast cancer cells. Nanoscale 16:16671–16683
15. Brouwer H et al (2025) Toxicity of true-to-life microplastics to human iPSC-derived intestinal epithelia correlates to their protein corona composition. J Hazard Mater 495:138908
16. Benjamin K et al (2024) Multiscale topology classifies cells in subcellular spatial transcriptomics. Nature 630:943–949
17. Qin Y et al (2021) A multi-scale map of cell structure fusing protein images and interactions. Nature 600:536–542
18. Das S, Vera M, Gandin V, Singer RH, Tutucci E (2021) Intracellular mRNA transport and localized translation. Nat Rev Mol Cell Biol 22:483–504
19. Hirose T, Ninomiya K, Nakagawa S, Yamazaki T (2023) A guide to membraneless organelles and their various roles in gene regulation. Nat Rev Mol Cell Biol 24:288–304
20. Mittag T, Pappu RV (2022) A conceptual framework for understanding phase separation and addressing open questions and challenges. Mol Cell 82:2201–2214

21. Bauer KE et al (2022) RNA supply drives physiological granule assembly in neurons. Nat Commun 13:2781
22. Majerciak V, Zhou T, Kruhlak MJ, Zheng Z-M (2023) RNA helicase DDX6 and scaffold protein GW182 in P-bodies promote biogenesis of stress granules. Nucleic Acids Res 51:9337–9355
23. Ripin N, de Vasconcelos L, Ugay DA, Parker R (2024) DDX6 modulates P-body and stress granule assembly, composition, and docking. J Cell Biol 223:e202306022
24. Riggs CL et al (2024) UBAP2L contributes to formation of P-bodies and modulates their association with stress granules. J Cell Biol 223:e202307146
25. Barrow ER et al (2024) Discovery of SQSTM1/p62-dependent P-bodies that regulate the NLRP3 inflammasome. Cell Rep 43:113935
26. Zong Y et al (2024) Mitochondrial dysfunction: mechanisms and advances in therapy. Signal Transduct Target Ther 9:124
27. Okkelman IA et al (2025) Visualizing the internalization and biological impact of nanoplastics in live intestinal organoids by Fluorescence Lifetime Imaging Microscopy (FLIM). Light Sci Appl 14:272
28. von Gerichten J et al (2024) Single-Cell Untargeted Lipidomics Using Liquid Chromatography and Data-Dependent Acquisition after Live Cell Selection. Anal Chem 96:6922–6929
29. Yang J et al (2025) Modular RNA interactions shape FXR1 condensates involved in mRNA localization and translation. Nat Commun 16:8589
30. Li T et al (2024) Blocker-SELEX: a structure-guided strategy for developing inhibitory aptamers disrupting undruggable transcription factor interactions. Nat Commun 15:6751
31. Wei W et al (2022) Anionic nanoplastic exposure induces endothelial leakiness. Nat Commun 13:4757
32. Villanueva E et al (2024) System-wide analysis of RNA and protein subcellular localization dynamics. Nat Methods 21:60–71
33. Zhang Z et al (2024) Unraveling Intracellular Protein Corona Components of Nanoplastics via Photocatalytic Protein Proximity Labeling. Anal Chem 96:4978–4986
34. Blake LA, Watkins L, Liu Y, Inoue T, Wu B (2024) A rapid inducible RNA decay system reveals fast mRNA decay in P-bodies. Nat Commun 15:2720
35. Kodali S et al (2024) RNA sequestration in P-bodies sustains myeloid leukaemia. Nat Cell Biol 26:1745–1758
36. Pessina P et al (2025) Selective RNA sequestration in biomolecular condensates directs cell fate transitions. Nat Biotechnol. 10.1038/s41587-025-02853-z
37. Adumeau L et al (2026) Condensate corona–nanoparticle complexes transfer functional biomolecules between cells. Nat Mater 25:1045–1057
38. Tan Y, Zhu X, Wu D, Song E, Song Y (2020) Compromised Autophagic Effect of Polystyrene Nanoplastics Mediated by Protein Corona Was Recovered after Lysosomal Degradation of Corona. Environ Sci Technol 54:11485–11493

39. Pachitariu M, Rariden M, Stringer C (2025) Cellpose-SAM: superhuman generalization for cellular segmentation. *bioRxiv* 2025.04.28.651001 10.1101/2025.04.28.651001
40. Gallusser B, Weigert M, Trackastra Transformer-based cell tracking for live-cell microscopy. https://github.com/
41. McInnes L, Healy J, Saul N, Großberger L (2018) UMAP: Uniform Manifold Approximation and Projection. J Open Source Softw 3:861
42. Patel H et al nf-core/rnaseq: nf-core/rnaseq v3.21.0 - Mercury Macaw. https://doi.org/10.5281/ZENODO.17153746
43. Ewels PA et al (2020) The nf-core framework for community-curated bioinformatics pipelines. Nat Biotechnol 38:276–278
44. Love MI, Huber W, Anders S (2014) Moderated estimation of fold change and dispersion for RNA-seq data with DESeq2. Genome Biol 15:550
45. Wu T et al (2021) clusterProfiler 4.0: A universal enrichment tool for interpreting omics data. Innovation 2:100141
46. Bailey TL et al (2009) MEME Suite: tools for motif discovery and searching. Nucleic Acids Res 37:W202–W208
47. Grant CE, Bailey TL, Noble W (2011) S. FIMO: scanning for occurrences of a given motif. Bioinformatics 27:1017–1018
48. Lorenz R et al (2011) ViennaRNA Package 2.0. Algorithms Mol Biology 6:26
49. Shen D et al (2026) Contrastive learning of dynamic processing body formation reveals undefined mechanisms of approved compounds. iScience 29:114866
50. Dominguez Mantes A et al (2025) Spotiflow: accurate and efficient spot detection for fluorescence microscopy with deep stereographic flow regression. Nat Methods 22:1495–1504

Figures

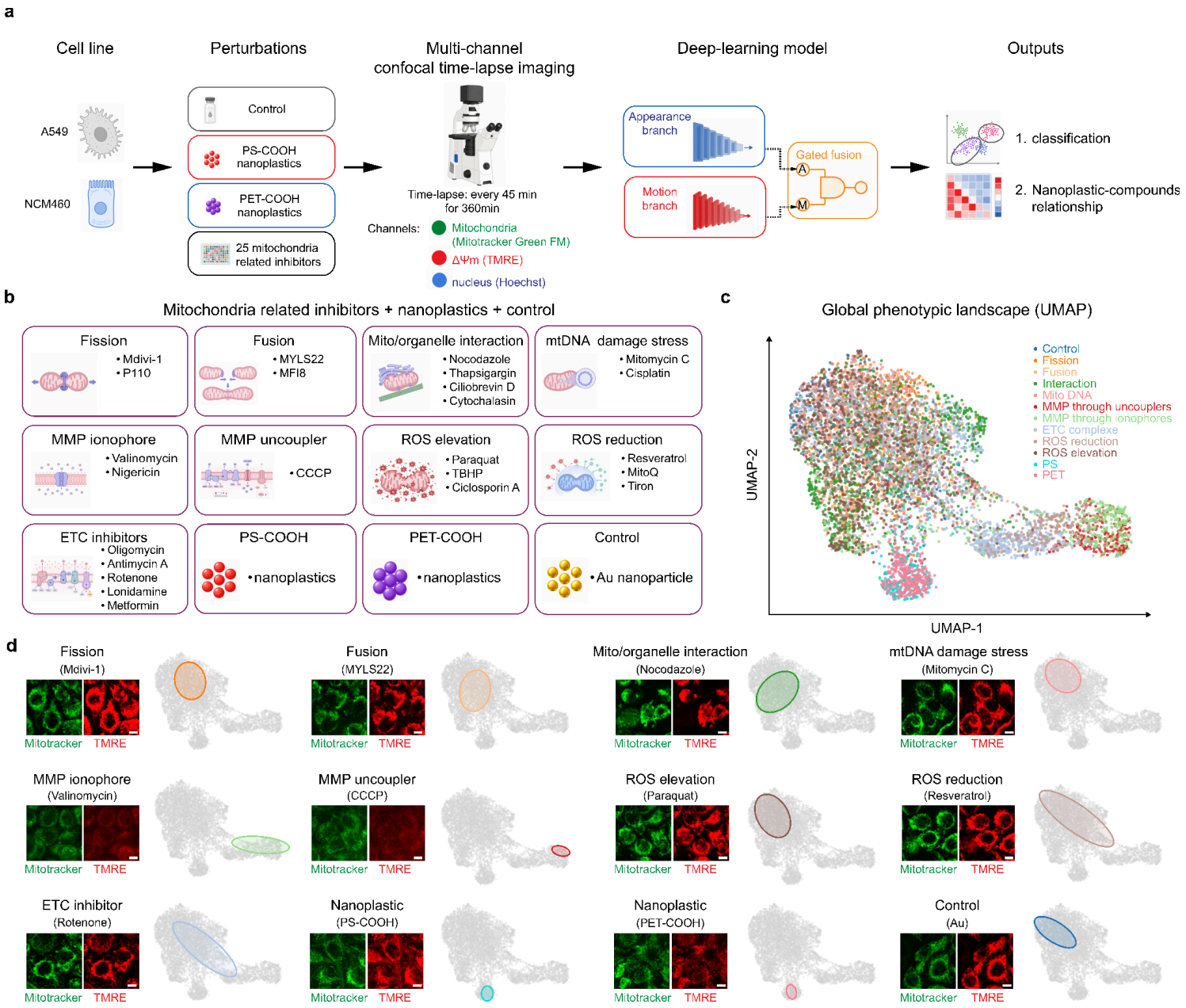


Figure 1

Image-based profiling distinguishes nanoplastic-associated phenotypes from reference mitochondrial perturbations.

(a) Schematic of the experimental and computational workflow. NCM460 and A549 cells were treated with 50-nm carboxylated polystyrene (PS-COOH) or polyethylene terephthalate (PET-COOH) nanoplastics, 50-nm Au nanoparticles, or 25 mitochondrial perturbagens, followed by multichannel confocal time-lapse imaging for 360 min. MitoTracker, TMRE, and Hoechst image sequences were analyzed using an appearance–motion fusion network that integrates features from single-cell z-slice image crops with dynamic features derived from optical-flow analysis. The resulting features were used for perturbation classification and phenotypic embedding.

(b) Perturbation panel. The 25 mitochondrial perturbagens were grouped according to their annotated target or stress category: fission, fusion, mitochondria–organelle interaction, mitochondrial DNA stress, mitochondrial membrane-potential disruption, electron-transport-chain inhibition and ROS modulation. Working concentrations for all perturbagens are listed in Supplementary Table 1.

(c) UMAP visualization of validation-set single-cell embeddings from NCM460 cells based on the final model features. Each point represents one cell and is coloured according to treatment class.

(d) Representative endpoint images of NCM460 cells at 360 min after the indicated treatments. MitoTracker and TMRE indicate mitochondrial morphology and membrane-potential-associated fluorescence, respectively. Images were individually contrast-adjusted for visualization. Scale bar, 10 μm.

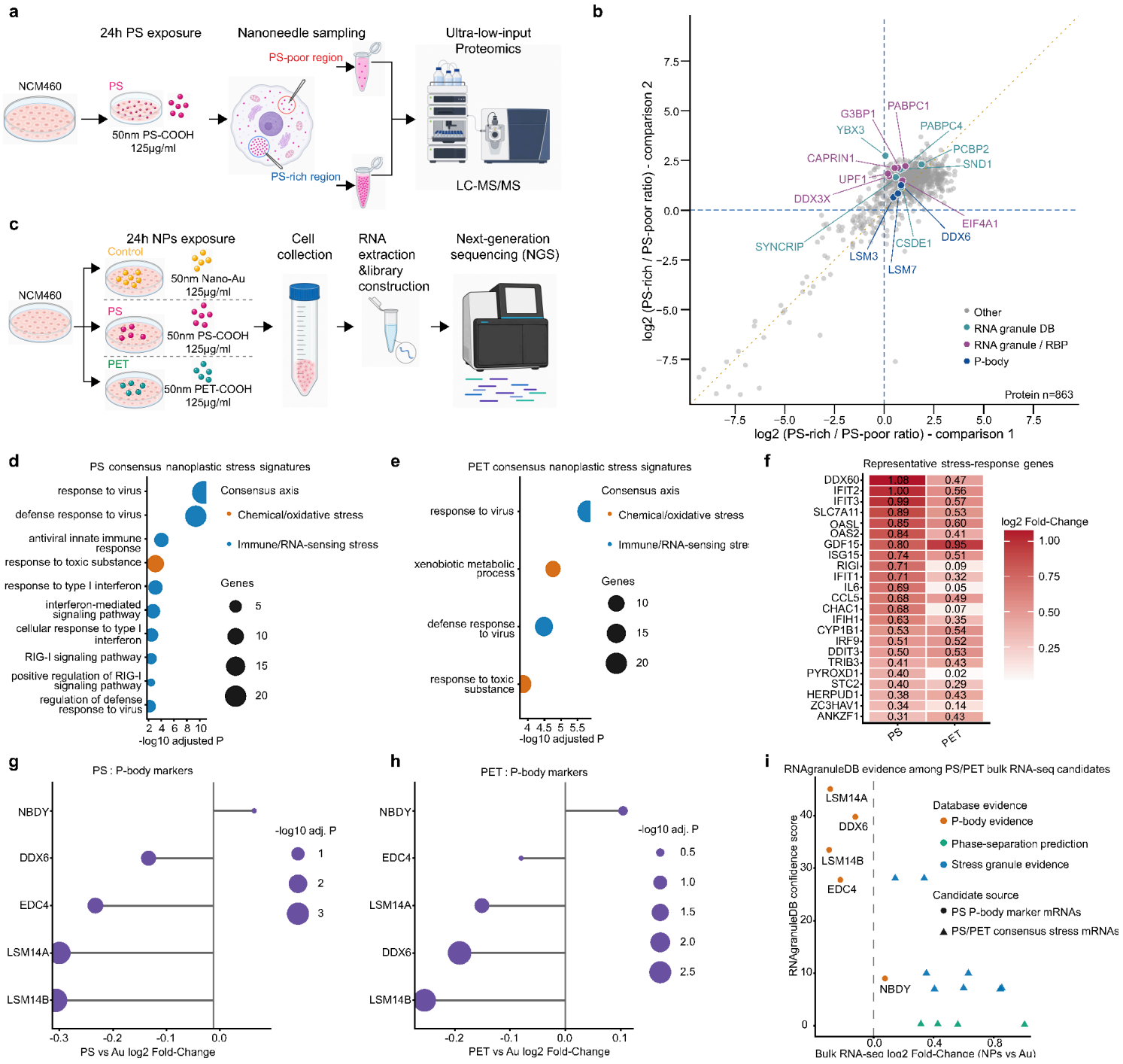


Figure 2

Regional proteomics identifies an RNP-associated molecular pattern distinct from the bulk nanoplastic stress response.

(a) Fluorescence-guided nanoneedle sampling workflow. NCM460 cells were exposed to 50-nm PS-COOH nanoplastics for 24 h, and fluorescence-defined PS-rich and PS-poor cytoplasmic regions were collected for ultra-low-input LC–MS/MS. Two pooled samples were analyzed per regional group, with each sample comprising six sampling regions.

(b) Pairwise abundance-ratio analysis of regional proteomics data. Each point represents one of 863 identified protein groups. Axes show log2-transformed PS-rich/PS-poor abundance ratios for the two pooled sample pairs. RNA-granule-, RNA-binding- and P-body-associated proteins were annotated using RNAgranuleDB.

(c) Bulk RNA-seq workflow. NCM460 cells were exposed for 24 h to Au nanoparticles, PS-COOH nanoplastics, or PET-COOH nanoplastics at 125 µg/ml before RNA extraction and sequencing. n = 3 biological replicates per group.

(d,e) Gene Ontology enrichment of stress-response genes induced by PS (d) or PET (e) relative to the Au nanoparticle control. Dot size indicates the number of genes, and color denotes the annotated stress-response axis.

(f) Heat map of representative nanoplastic-responsive stress genes. Values indicate log2 fold changes relative to the Au nanoparticle control.

(g,h) Bulk RNA-seq analysis of canonical P-body marker transcripts following PS (g) or PET (h) exposure. The x-axis shows log2 fold change relative to the Au nanoparticle control, and point size indicates −log10-adjusted P value. The marker set did not show coordinated transcriptional induction.

(i) RNAgranuleDB annotation of PS- and PET-responsive transcript candidates. The x-axis shows bulk RNA-seq log2 fold change relative to the Au nanoparticle control, and the y-axis shows the RNAgranuleDB confidence score.

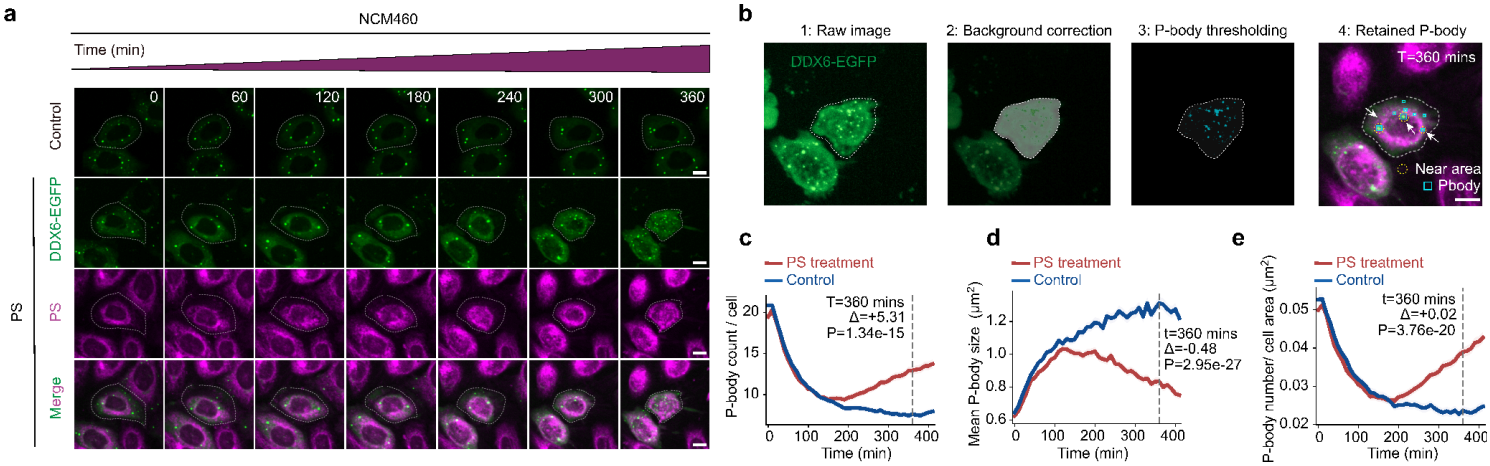


Figure 3

Live-cell imaging reveals nanoplastic-associated remodeling of DDX6-positive P-bodies.
(a) Representative DDX6–EGFP live-cell time-lapse images of NCM460 cells exposed to Au nanoparticles or polystyrene (PS) nanoplastics. For PS-treated cells, DDX6–EGFP, PS fluorescence, and merged images are shown. Time indicates minutes after particle addition. Scale bar, 10 µm.

(b) Image-analysis workflow for detection and quantification of DDX6–EGFP-positive P-body puncta, including background correction, intensity thresholding and retention of detected puncta. The region used to quantify local PS fluorescence around each punctum is indicated.

(c) Time-resolved DDX6-positive P-body punctum number per cell in NCM460 cells.

(d) Time-resolved mean area of DDX6-positive P-body puncta per cell in NCM460 cells.

(e) Time-resolved DDX6-positive P-body punctum density in NCM460 cells, calculated as punctum number normalized to segmented cell area.

For c–e, lines show pooled-cell means and shaded regions indicate s.e.m. At 360 min, Δ denotes the mean value in the PS-treated group minus that in the Au-treated group. n = 428 PS-treated cells and 393 Au-treated cells. P values were calculated using two-sided Mann–Whitney U tests, with individual cells treated as the observational unit.

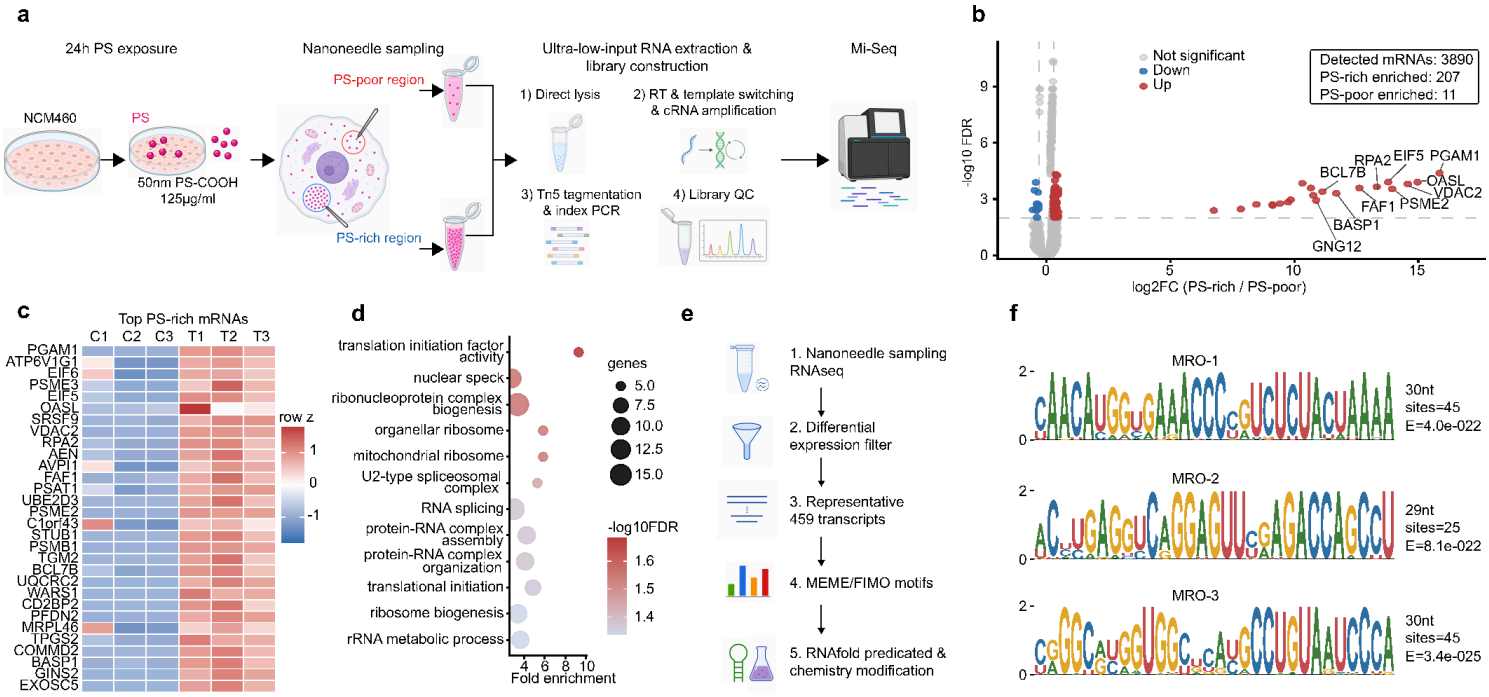


Figure 4

Nanoneedle RNA-seq identifies mRNA signatures in PS-enriched cytoplasmic regions and guides motif-derived RNA oligonucleotide design

(a) Workflow for fluorescence-guided nanoneedle sampling and low-input RNA-seq of NCM460 cytoplasmic regions with low or high PS fluorescence after PS-COOH exposure. n = 3 local RNA-seq samples per regional group.

(b) Volcano plot showing transcript enrichment in PS-rich relative to PS-poor regions. At the indicated thresholds, 207 genes were enriched in PS-rich regions and 11 in PS-poor regions. Labeled genes

represent the ten most highly expressed genes among the transcripts enriched in PS-rich regions.

(c) Heat map of representative transcripts enriched in PS-rich regions. Values are row-scaled log10-transformed counts.

(d) Gene Ontology enrichment of RNA-processing, translation and ribonucleoprotein-complex terms among genes enriched in PS-rich regions. Dot size indicates the number of genes, color denotes −log10 false-discovery rate, and the x-axis shows fold enrichment.

(e) MRO-selection workflow. A broader set of 459 upregulated transcript sequences was used for motif discovery with MEME and motif scanning with FIMO, followed by selection of representative motif-containing sequences and RNAfold-based secondary-structure prediction.

(f) Motif logos corresponding to MRO-1, MRO-2 and MRO-3, generated from MEME probability matrices derived from the 459 transcript sequences.

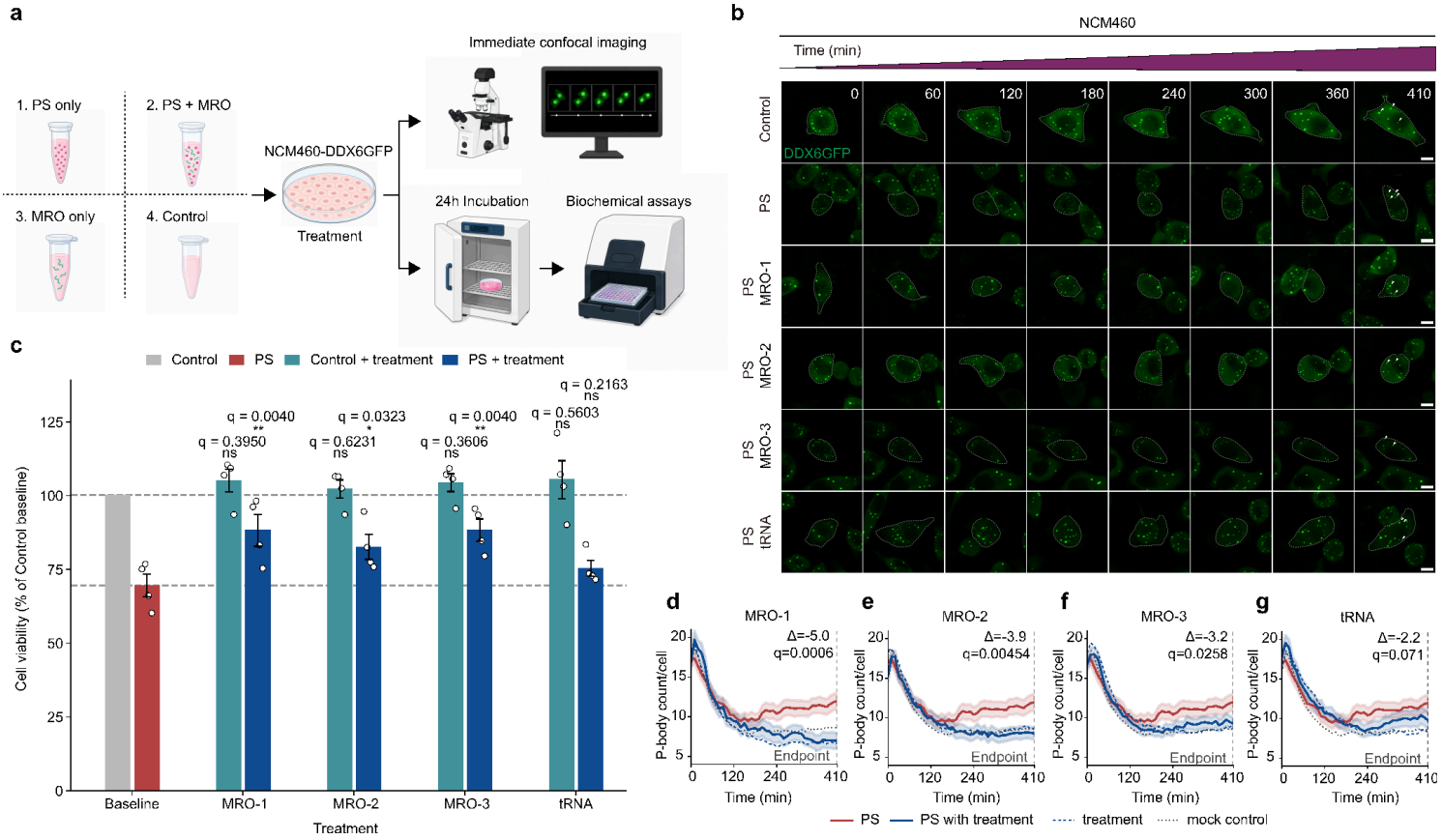


Figure 5

Motif-derived RNA oligonucleotides modulate PS-associated P-body remodeling and cell viability.

(a) Experimental design. NCM460 cells stably expressing DDX6–EGFP were treated with 50-nm PS-COOH nanoplastics (125 μg/ml), the indicated motif-derived RNA oligonucleotide (MRO) or control tRNA

(500 nM), both, or neither. Live-cell confocal imaging was initiated immediately after treatment, and cell viability was measured independently after 24 h.

(b) Representative DDX6–EGFP live-cell confocal time-lapse images of mock control, PS alone, and PS plus the indicated RNA treatments from 0 to 410 min. Dashed contours indicate segmented cell boundaries, and white arrowheads indicate representative DDX6-positive puncta. Scale bar, 10 μm.

(c) Cell viability after 24 h under control or PS conditions in the presence of MRO-1, MRO-2, MRO-3 or tRNA. Within each biological replicate, values were normalized to the untreated control. Bars show mean ± s.e.m., and open circles represent individual biological replicates. For each RNA, RNA-alone conditions were compared with the untreated control, and PS-plus-RNA conditions were compared with PS alone, using two-sided paired t-tests with Benjamini–Hochberg adjustment across comparisons. n = 4 biological replicates.

(d–g) Time-resolved DDX6-positive punctum number per cell following treatment with MRO-1 (d), MRO-2 (e), MRO-3 (f) or tRNA (g), with or without PS. Red, solid blue, dashed blue and dotted grey lines denote PS alone, PS plus RNA, RNA alone and mock control, respectively. Lines show pooled-cell means and shaded regions indicate s.e.m. At 410 min, PS-alone and PS-plus-RNA groups were compared using two-sided Mann–Whitney U tests with Benjamini–Hochberg adjustment across the four RNA conditions; exact q values are shown in the panels. Δ denotes the mean value in the PS-plus-RNA group minus that in the PS-alone group. Cell numbers for PS alone, PS plus RNA, RNA alone and mock control, respectively, were: d, 65, 48, 116 and 124; e, 65, 76, 151 and 124; f, 65, 85, 134 and 124; and g, 65, 73, 138 and 124.

Supplementary Files

This is a list of supplementary files associated with this preprint. Click to download.

- Supplementalinformationtitlesandlegends.docx
- SupplementaryTable1.xlsx
- SupplementaryTable2.xlsx
- SupplementaryTable3.xlsx
- Pangetal20260814DocumentS1.docx